World Scientific
www.worldscientific.com

JAPAN SOCIETY OF CIVIL ENGINEERS
COASTAL ENGINEERING COMMITTEE

Coastal Engineering Journal, Vol. 58, No. 1 (2016) 1640004 (25 pages)

DOI: 10.1142/S0578563416400040

Observations and Modeling of Coastal Boulder Transport and Loading During Super Typhoon Haiyan

Andrew B. Kennedy[*,¶], Nobuhito Mori[†], Yao Zhang[*], Tomohiro Yasuda[†], Shen-En Chen[‡], Yoshimitsu Tajima[§], William Pecor[*] and Kinya Toride[§]

[*]*Department of Civil and Environmental Engineering and Earth Sciences, University of Notre Dame, Notre Dame, IN, USA*

[†]*Disaster Prevention Research Institute, Kyoto University, Uji, Kyoto, Japan*

[‡]*Department of Civil and Environmental Engineering, University of North Carolina, Charlotte, NC, USA*

[§]*Department of Civil Engineering, University of Tokyo, Tokyo, Japan*

[¶]*andrew.kennedy@nd.edu*

Received 17 March 2015
Accepted 29 September 2015
Published 6 January 2016

Boulders numbering in the high hundreds/low thousands, and with masses up to ~ 30 tonnes, were transported onshore by Super Typhoon Haiyan in Calicoan Island, Philippines to maximum ground elevations that could exceed 9 m and terminal positions up to ~ 180 m inland. One-dimensional Boussinesq hindcasts of coastal boulder motion showed intermittent transport initiated at the fronts of infragravity swash bores. Transport distances were found to be highly sensitive to wave-height, enough so that observations of terminal positions may be a viable method of estimating rough paleostorm magnitudes. The large accelerations at bore fronts generated significant inertial forces, particularly for larger boulders, but drag forces had greater root-mean-square magnitudes in all simulations. Widely used relations to infer fluid velocities from boulder properties were tested using modeled boulders — inferred velocities at modeled terminal boulder positions were compared to maximum computed Boussinesq fluid velocities at these locations and found to be significantly lower. This underprediction of inferred velocities was greatest for smaller boulders that were strongly mobile. Inferred drag loads compared to modeled values were somewhat more accurate for large boulders when a Froude number of unity was assumed to estimate flow depths. Although these boulders were unequivocally transported by storm waves, their large sizes and distances traveled venture into what has been considered the tsunami range. Thus, care must be taken to interpret the provenance of coastal boulder fields with unknown origin for lower to mid-latitude regions.

Keywords: Typhoon Haiyan; boulder transport; Boussinesq equations; surf zone; infragravity waves.

1. Introduction

The transport of coastal boulders by storm waves and tsunamis has been a topic of considerable discussion in the recent literature [Nott, 2003; Fichaut and Suanez, 2011; Lorang, 2011; Engel and May, 2012; Bourgeois and MacInnes, 2010]. In large part, the motivation for these boulder transport studies has been to estimate the magnitude of past events for which no other records exist [Nott, 2003; Nandasena *et al.*, 2011], and to evaluate implications for present day disaster reduction planning. However, there is often considerable uncertainty in these estimates: the local magnitudes of water velocities and depths leading to transport; the overall event magnitudes; and even whether the observed transport was caused by storm waves or by a tsunami, as many coastlines are affected by both phenomena. Because it is important to understand the source of existing boulders in these areas, the large number of high magnitude storm events storm events compared to tsunamis may provide opportunities to test boulder transport models.

One of the greatest uncertainties in these studies is the quantification of hydrodynamics leading to transport. The presence of storm-transported boulders can be used to directly infer the hydrodynamics leading to their transport [Nott, 2003], although with uncertain accuracy. These hydrodynamic conditions are also directly related to structural loads of interest to engineers and planners. However, reconstructions of past events tend to use quite simplified hydrodynamics and forces acting on boulders [Nott, 2003; Engel and May, 2012; Bourgeois and MacInnes, 2010], and make little allowance for hydrodynamic interactions with local topography. Fortunately, many numerical tools exist that can simulate the detailed transformation of either tsunamis or storm waves over coastal topographies, and the resulting water depths and velocities leading to boulder transport. Some recent studies have employed hydrodynamic models to simulate conditions during tsunamis [e.g. Nandasena *et al.*, 2013; Sugawara *et al.*, 2014], which can then be used to drive dynamical boulder transport models and compared with measurements. In principle, magnitudes of unknown tsunamis or storms could be estimated by comparing modeled and observed transport characteristics and determining a best match. Alternatively, models could be used to distinguish between storms or tsunamis [e.g. Buckley *et al.*, 2012]. However, there are many uncertainties in this type of analysis, and accuracy remains to be evaluated.

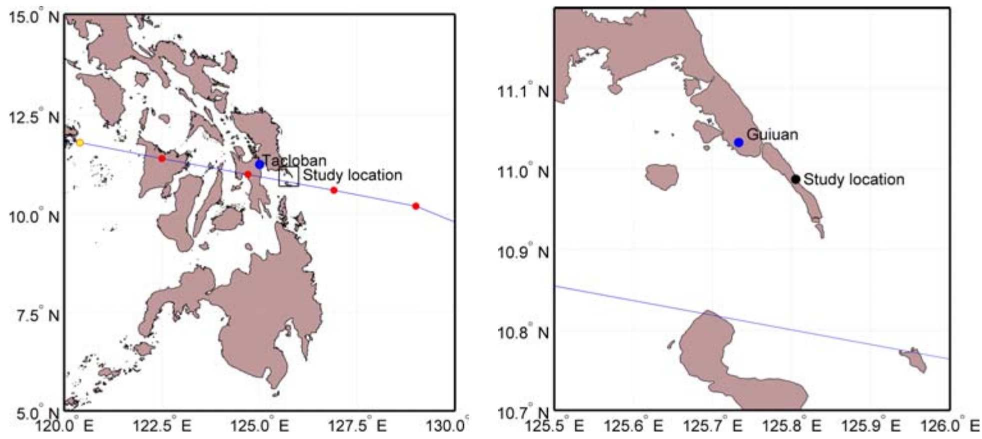

(a) (b)

Fig. 1. (a) Track of Super Typhoon Haiyan, and study location. (b) Close-up of study location on Calicoan Island.

Super Typhoon Haiyan (locally referred to as Yolanda), with track shown in Fig. 1(a), made landfall just south of Samar Island in the Philippines at around 2100UTC, 7 November 2013. Haiyan may have been the strongest storm to make landfall in the modern satellite era, with the Joint Typhoon Warning Center [2013] estimating maximum one minute sustained winds of 170 knots (195 mph) shortly before landfall. More than 6000 fatalities have been verified, and hundreds of thousands of structures were damaged or destroyed by the storm. Storm surge of 5–6 m was measured and modeled in the Gulf of Leyte, with wave runups exceeding 10 m on the open Pacific coast [Mori *et al.*, 2014; Tajima *et al.*, 2014]. This large runup was possible because the ocean east of Samar drops steeply into the 10,000 m deep Philippine Trench with no land for thousands of km to the east: thus, large waves generated during Haiyan were able to propagate very close to the Eastern Samar shoreline before dissipating. The region is microtidal, with mean tide ranges of O(1 m). Because of the deep offshore bathymetry in the Philippine Trench, the coastal storm surge in Eastern Samar was quite low, with maximum hindcast elevation anomalies less than 0.3 m [Mori *et al.*, 2014].

This paper examines boulder transport during Super Typhoon Haiyan using direct observations of post-storm conditions combined with phase-resolving numerical Boussinesq models of runup hydrodynamics driving boulder transport. This work confines itself to transport in the vicinity of sandy beaches: large boulder transport that was observed on nearby clifftops during Haiyan lies beyond the scope of this paper, but will be discussed elsewhere.

2. Observed Boulder Transport

The study site on Calicoan Island is located at the southeastern tip of Samar Island facing the Pacific Ocean as seen in Fig. 1(b). Eastern Samar has a humid tropical climate with greater than 3 m average annual rainfall (http://pagasa.dost.gov.ph) and is lightly developed, with fishing and agriculture as major industries. The shoreline near the study site is characterized by low limestone cliffs and headlands with elevations 5–10 m, separated by high gradient, narrow sand beaches. Almost completely level fringing reefs border much of the coast, with typical widths of several hundred meters in front of sand beaches, and with much smaller widths (or none) seaward of cliffs and headlands. The underlying limestone is highly weathered, with very sharp Karst topography on headlands in the direct sea spray region, and slightly more subdued weathering further inland. Numerous caves are found in this immediate area [Husana and Yamamuro, 2013]. The study site is at the far northern extent of the approximately 2.4 km Ngolos beach on the Pacific (eastern) coast of Calicoan Island. As shown in Fig. 2(a), the beach section is bounded by a large rocky headland to the north and bisected by a smaller spur. The southern portion of the study area has a ∼200 m wide fringing reef that decreases in width with distance north, and vanishes at the northern headland. This beach experienced around 50 m of erosion during Haiyan, in some places down to bedrock. Vegetative overwash debris (mostly coconut palms) were found more than 200 m inland at around 9 m above sea level (ASL) on both the beach plain and the northern headland. Along transect T1, the foreshore beach itself is very steep, with an average slope of 0.09 for the first 90 m from the shoreline, and a much more gentle 0.01 slope for the next 120 m. The beach was the site of a small seaside development, with concrete roads

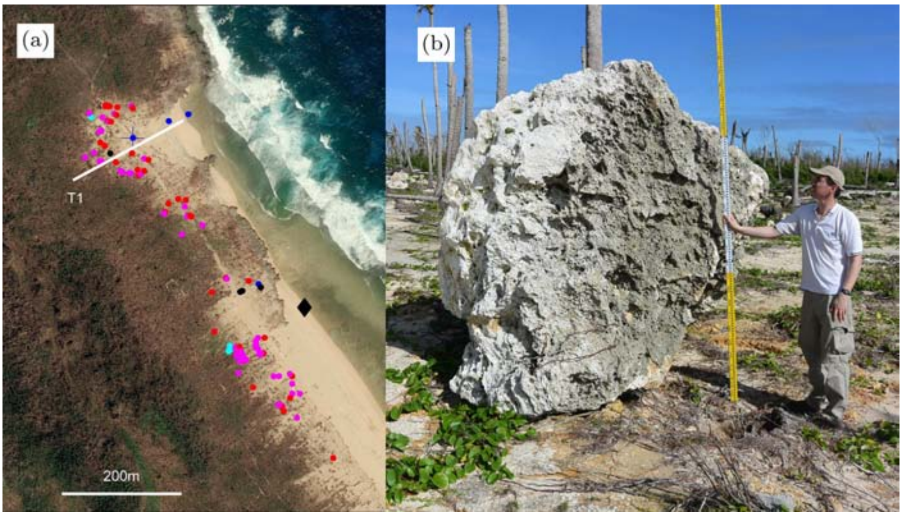

Fig. 2. (a) Study location showing cross-shore transect T1 (with elevation profile given in Fig. 8(b)) and surveyed boulder locations colored by size. (•) $D > 2$ m; (•) 1.5 m $< D \leq 2$ m; (•) 1 m $< D \leq$ 1.5 m; (•) 0.5 m $< D \leq$ 1 m; (•) $D <$ 0.5 m; (+) Location of boulder in Fig. 2(b); (◆) Location of photo in Fig. 3. Background image taken December 15, 2013 from Pleiades 1B satellite. (b) The largest boulder (ID 77), found at ∼8 m ASL along transect T1.

and foundation slabs along its length, some small beach cabins, and many coconut palms. No structures survived the storm in this location.

Storm-transported boulders numbering in the high hundreds/low thousands (characteristic size $D \equiv (abc)^{1/3} > 256\,\text{mm}$, with a, b, c the three boulder axial length scales) were found all along the northern section of the beach, both along the beach plain and against the headlands. The total number of boulders could not be accurately determined both because of the large quantity and because many were obscured by vegetation. Of those visible, 118 were surveyed for size (a, b, c axes), location, and visual properties in detail. A straight line was fit to the overall mean sea level sandy beach shoreline post-Haiyan over the study area, and boulder positions from shoreline, x, (onshore positive) were measured from this line. Because not all boulders could be surveyed, many of the largest visible boulders in an area were chosen, plus large boulders found near the inland extent of travel. Small boulders with characteristic dimensions $D < 1\,\text{m}$ in particular are highly underrepresented in this survey, as they were neglected in favor of larger boulders, but these smaller boulders were visually the most abundant as shown in Fig. 3. Boulders were transported at varying distances inland: few large boulders were moved more than $\sim 180\,\text{m}$ from the shoreline. Probably not coincidentally, this was also the approximate location where vegetation became extremely thick and tangled, and was near the ~ 200–$220\,\text{m}$ inland limit of large rafted debris such as palm logs. Many smaller boulders with $D < 1\,\text{m}$ were observed to be trapped at the break in slope between the flat reef and the steep foreshore slope (Fig. 3).

All boulders examined were composed of calcium carbonate: the large majority appeared to derive from the same limestone as the heavily weathered headland, while

Fig. 3. Small boulder concentration at the break in slope between reef flat and steep foreshore beach with the first author. The photo location is shown in Fig. 2(a).

Fig. 4. (Color online) Examples of boulder types observed on Calicoan Island. Clockwise from top left: pink iron oxide-stained boulder; weathered gray boulder with likely subaerial near-shoreline origin; white boulder with weakly cemented gravel attached (originally on lower side); white boulder rounded by water.

Fig. 5. (Color online) Distribution of (a) Pink/Orange; and (b) White/Gray boulders. Boulders with more than one major color are shown on both plots.

the origin of others was indeterminate. Some boulders were clearly of subaqueous origin, while others appeared to be subaerial, with attached roots. Some pink or orange boulders with iron oxide staining appeared to have been buried pre-storm and became mobile when the beach eroded, many having terminal positions in much higher elevation non-eroded areas. Figure 4 gives examples of some of the different boulder types found, while Fig. 5 shows individual locations as a function of color. Interestingly, all pink/orange boulders were found inland from sandy portions of the study site, providing further evidence of their pre-storm burial. In contrast, white/gray boulders were not confined to these locations, but were also found on headlands. The many boulders observed along the post-storm beach suggest that, if the beach eventually recovers to its pre-storm position, these will be buried over time and may become mobile during a future storm.

Many boulders (71/118 measured) were found near obstructions (trees and vegetation, foundations, other boulders, headlands) that may have impeded their progress. Long (a) axes were often parallel to the shoreline, and short (c) axes vertical, but this was not always the case. The largest subaerial boulder as shown in Fig. 2(b) was quite irregular, with estimated mass of 30 tonnes (calculated using $m = 0.5\rho_s abc$, see Engel and May [2012]). It was found resting partially on a road at 8 m ASL, and may have originated just offshore at around $x = -25$ m, where $x = 0$ m gives the nominal shoreline. Several large boulders could be seen in pre-storm satellite photos presented in Fig. 6 but were not at this location in post-storm images or post-storm ground reconnaissance. These large boulders may also have broken during the storm to become the source for smaller boulders, but it is not possible to say with certainty.

Elevations above sea level shown in Figure 8 were measured using a rod and level on transect T1 with location in Fig. 2. Elevations below sea level were estimated from wading, sea color and wave breaking locations on satellite photographs, and are much more approximate. Depths beyond the breaker line were assumed to drop off steeply as shown in nautical charts, and no evidence of wave transformation could be seen in

Fig. 6. (Color online) Pre-storm satellite photograph at northern end of study site showing two large boulders that were not in the same locations post-storm.

satellite photos to support a more gentle increase in depths. Figure 8b shows transect elevations, with a 60 m maximum depth used to accommodate the hydrodynamic modeling. This transect had water-smoothed rock at the lowest elevations above sea level, and sand and vegetation at higher elevations.

3. Hydrodynamic Modeling of Boulder Transport

The case of Super Typhoon Haiyan provides an opportunity to increase understanding of boulder transport during severe storms by linking the storm characteristics, nearshore waves and surge climate, and corresponding boulder transport. Haiyan had some (although not complete) information about the storm and conditions that may be used to model boulder transport and its sensitivity to hydrodynamic conditions. Models may also be used to test widely used inferences of the maximum fluid velocity experienced by a site. Finally, links between boulder transport and structural loads can provide important information for planning and design.

Modeling of boulder transport has three components: (1) Characterization of the incident wave climate and storm surge; (2) Modeling wave transformation through the surf and swash zones; and (3) Using detailed hydrodynamic time series to predict forces on boulders, and thus to drive boulder transport.

3.1. *Wave and surge modeling from deep water through the surf and swash zones*

Typhoon Haiyan was hindcast using the Weather Research and Forecasting (WRF) model [Skamarock *et al.*, 2008] for atmospheric modeling; multi-domain nesting and data assimilation using spectral nudging (SN) were applied to simulate typhoon characteristics correctly. The domain size of WRF was approximately 4000×2000 km centered at 130°E and 10°N and the minimum spatial resolution selected for WRF was 1 km. Initial, lateral, and sea surface boundary conditions were taken from the Final Operational Global Analysis by the National Centers for Environmental Prediction and Japan Meteorological Agency's Global Spectral Model, respectively. Storm surge and wind waves were simulated using the surge-wave coupling model [Kim *et al.*, 2009] combining a nonlinear shallow water equation and the spectral wave model SWAN [Booij *et al.*, 1998]. Atmospheric and surge-wave modeling used the same size domain, and three-level, two-way nesting was performed with spatial resolution up to 0.00667°. Wave radiation stresses were computed from the spectral wave model and fed into the shallow water model. A series of computations was performed by changing numerical setup and boundary conditions; accuracy of the typhoon, storm surge, and wave hindcast has been validated by satellite and other available data [Mori *et al.*, 2014]. We selected the best hindcast results from the ensemble.

Figure 7 shows hindcast significant wave-height, peak period, and surge + tide level in deep water just offshore of the boulder site. Significant wave-heights reached

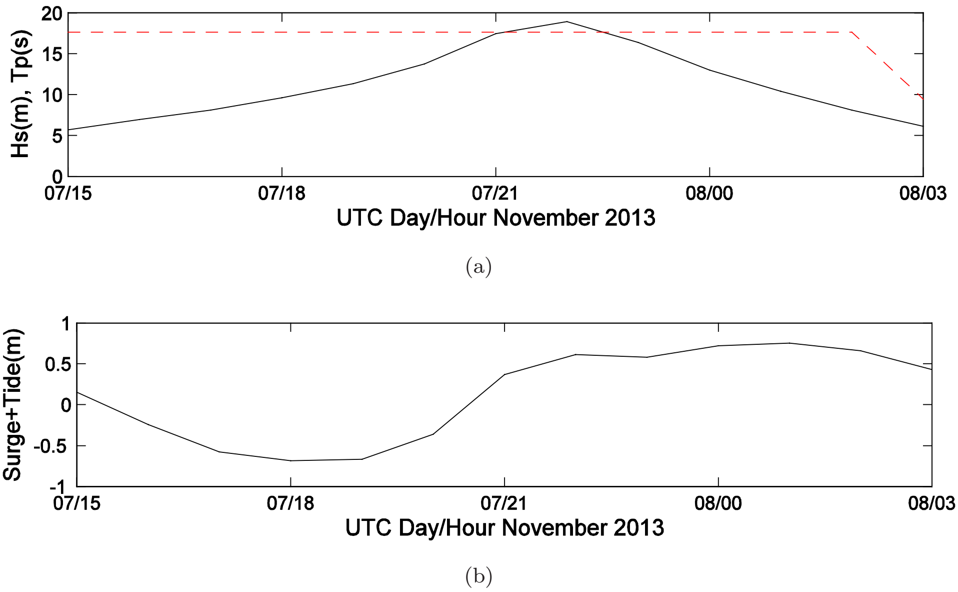

Fig. 7. (Color online) (a) Hindcast significant wave height (black) and peak period (red); (b) Hindcast offshore water surface elevation.

$H_s^{\max} = 18.9\,\mathrm{m}$, while surge was very low. The low surge is not a surprise, as the extremely deep water offshore of the study site reduced wind surge greatly, with barometric effects the only remaining contribution. High waves are also not a surprise: although there is no direct validation of heights for this storm, waves in this extreme height range have been observed at other locations [Cardone *et al.*, 2015]. In addition to boulder transport, 12.2 m wave runup during Haiyan was also measured at this location [Shimozono *et al.*, 2015].

Local wave transformation and runup were computed using a one-dimensional Boussinesq–Green–Naghdi wave model [Zhang *et al.*, 2013, 2014] over transect T1 with input time series of random waves with JONSWAP spectrum, and wave properties and surge heights taken from the larger scale hindcast. A grid size of 4 m and time step of 0.04 s were used. Because the random phase used to generate wave time series can have a significant impact on wave runup, 20 simulations were carried out, each using different random seeds for wave phases. Output time series of water depth and velocities were then used to compute loads and drive boulder motion in a one-way sense: i.e. waves and surge affected boulders, but boulders did not influence hydrodynamics.

Figure 8 shows the transformation of significant wave height over the strongest hour of the storm (2200 UTC, 21/11/2013) from the constant depth offshore region through to the shoreline. Significant wave height was retrieved from output time series of water surface elevations using $H_s = 1.416 \times 8^{1/2}\sigma_\eta$, where η is the standard deviation of surface elevation at a given location [Dean and Dalrymple, 1991]. As expected, wave heights decrease strongly with decreasing offshore depths, and then

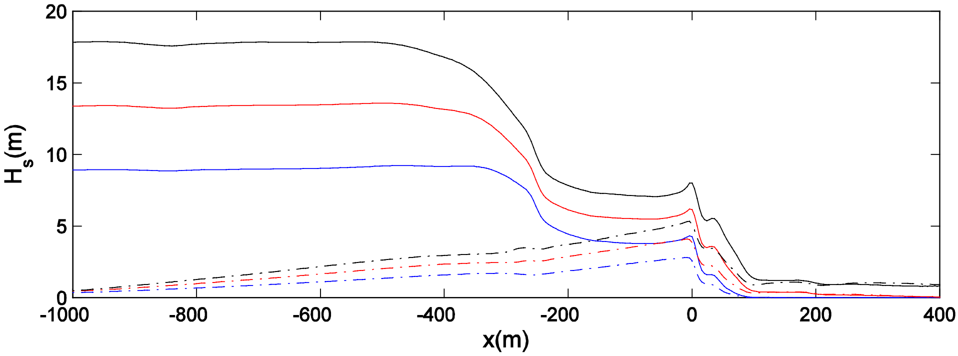

(a)

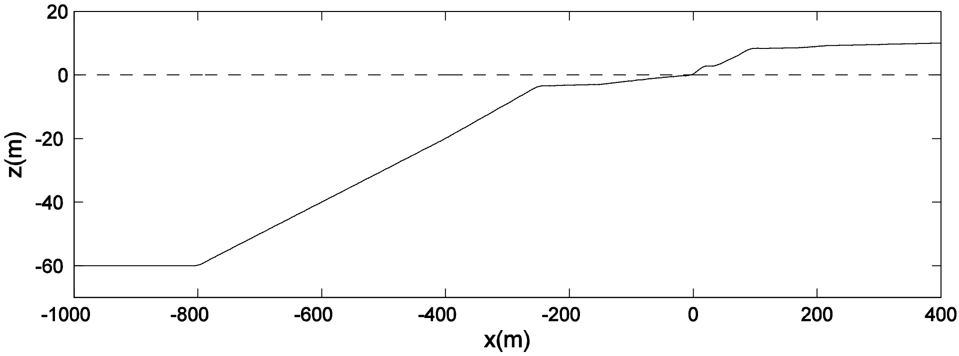

(b)

Fig. 8. (a) (–) Significant wave height; and (–•–) significant infragravity wave height over strongest hour of Boussinesq computations for input wave conditions (—) 1.0 Hs, (—) 0.75 Hs, (—) 0.5 Hs; (b) Bathymetry and topography used for wave and boulder transport computations.

become much smaller in the normally dry runup region. Significant wave heights of just under 1 m are seen at the onshore boundary of the simulation, showing that runup regularly reached the boundary with significant force, which is a prerequisite for boulder transport. Infragravity significant wave heights, defined here as having periods greater than 30 s, are also shown here. Infragravity heights are quite small offshore, but increase strongly in the breaking and runup regions and dominate in the flatter region with $x > 150$ m. Both the importance of infragravity components in the inner surf and swash zones, and their dominance on flat areas are in agreement with many other studies [e.g. Nwogu and Demirbilek, 2010; Stockdon and Holman, 2006]. These low frequency components allow loads to act for much longer than is possible from shorter period incident waves, and increase both the distance of inundation over an infragravity period and the distance a boulder could travel.

Additional simulations of wave transformation and runup were performed over the course of the storm using $0.75H_s$ and $0.5H_s$ hindcast wave heights to drive the Boussinesq model, and are shown in Fig. 8(a). Wave transformation through to the still water shoreline at $x = 0$ shows expected behavior, with smaller heights than with the original simulation. Low frequency motions also increase strongly in the surf and runup zones as with the original simulation. However, runup heights are both much smaller and do not extend as far inland and to as high elevations. Thus, larger incident waves not only provide significantly greater forcing to any boulders offshore or near the still water level, but will also have forcing in onshore locations that can not be reached by the smaller waves. Because the runup itself is a signature of storm size, and because boulders can only be driven to the limit of runup, the maximum inland penetration of observed boulders will provide an additional measure of storm intensity. This reduction of inundation with decreasing wave height [e.g. Shimozono *et al.*, 2015] may prove an important tool when attempting to evaluate the intensity of historic storms using boulder transport signatures.

Figure 9(a) shows time series of runup likely to cause boulder motion (defined here as $x_{0.75}$, the furthest shoreward position with instantaneous water depth greater than 0.75 m, which could be sufficient to drive motion for smaller boulders) over the

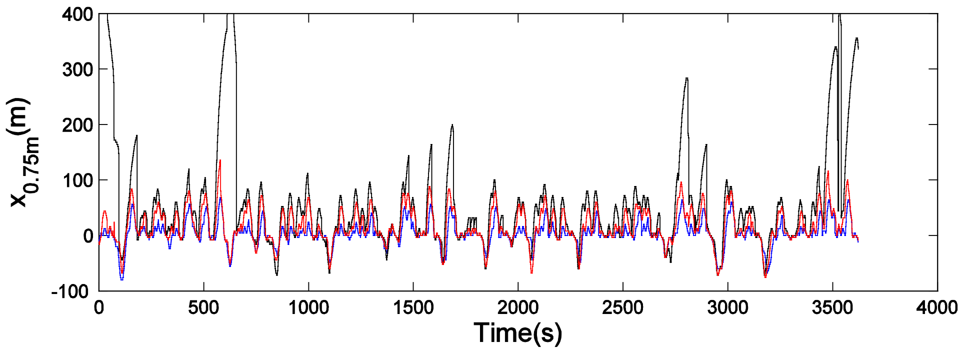

(a)

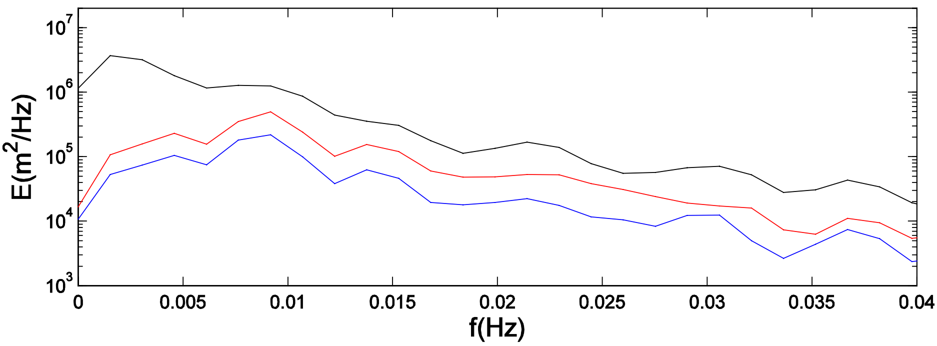

(b)

Fig. 9. (a) Time series of runup horizontal distance over the strongest hour of the storm using incident wave heights (—) 1.0 Hs, (—) 0.75 Hs, (—) 0.5 Hs; (b) Spectral densities for the runup time series of (a).

strongest hour of the storm for the three initial wave heights 1.0 Hs, 0.75 Hs, and 0.5 Hs. All three simulations use identical random phase information, so the incident wave signals are scalar multiples; thus runup signals are also highly coherent. Runup time series for the three heights are generally quite similar, with the largest waves generating the largest runup. All three wave heights show a strong infragravity signal: although incident waves have a peak period of $T_p = 17.7\,\mathrm{s}$, spectral analysis of the runup time series shown in Fig. 9(b) shows much longer peak periods of [654 s, 109 s, 109 s] for [1.0 Hs, 0.75 Hs, 0.5 Hs]. While all of these represent strong frequency downshifts, the waves using 1.0 Hs have an extremely long peak period arising from the large excursions that occur when runup reaches the flatter portion of the domain, and can propagate inland very easily. Runup from the smaller wave heights 0.75 Hs and 0.5 Hs can not as easily reach this more elevated region, and thus do not show such large excursions or such extreme frequency downshifts. As mentioned previously, this increase in low frequency energy has strong implications for boulder transport as the much longer period flows significantly increase capacity for long distance transport.

3.2. *Boulder transport modeling*

The model for boulder motion was adapted from Imamura *et al.* [2008]. The basic equation of motion for boulders was

$$\frac{\partial^2 X}{\partial t^2} = (F_d + F_i - F_g - F_f)/[\mathrm{Vol}_s(C_m - 1)\rho_w + \mathrm{Vol}_0\rho_s], \tag{1}$$

where X was the boulder cross-shore coordinate, F_d was the drag force, F_i was the inertial force, F_g was the gravitational component along the slope, and F_f was the frictional drag force. The submerged volume of the boulder was Vol_s while the total volume of the boulder was Vol_0. Bulk densities of water and rock were ρ_w and ρ_s, respectively, while C_m was the inertial coefficient. If the boulder was stationary and $|F_d + F_i - F_g| \le |F_f|$, then $\partial^2 X/\partial t^2 = 0$. Initiation of rolling criteria were not used in this model, implying sliding motion (which is known to not be true for some observed boulders).

Drag force (F_d), inertial force (F_i), gravitational force (F_g), and frictional force (F_f) were given by:

$$F_d = 0.5\rho_w A_s U|U|, \tag{2}$$

$$F_i = \rho_w C_m \mathrm{Vol}_s \frac{DU}{Dt}, \tag{3}$$

$$F_g = -(-\rho_w g\,\mathrm{Vol}_s + \rho_s g\,\mathrm{Vol}_0 - F_L)\sin\theta, \tag{4}$$

$$F_f = \mu(-\rho_w g\,\mathrm{Vol}_s + \rho_s g\,\mathrm{Vol}_0 - F_L)\cos\theta, \tag{5}$$

where A_s was the submerged frontal area, U was the depth-averaged fluid velocity at the boulder location (taken from Boussinesq simulations), and θ was the beach slope angle in radians. Different friction coefficients are given when the boulder is stationary, $\mu = \mu_0$, or when in motion, $\mu = \mu_d$. The lift force was given as

$$F_L = 0.5 C_l \rho_w a[0.5(b+c)] \left(U - \frac{\partial X}{\partial t}\right)^2 \min\left(2.5\frac{h+\eta}{0.5(b+c)}, 1\right), \quad h+\eta > 0.5(b+c) \tag{6}$$

and $F_l = 0$ otherwise. The factor $\min(2.5\frac{h+\eta}{0.5(b+c)}, 1)$ allows for a smooth transition between no lift and full lift from 1 to 2.5 boulder depths of water.

Because many coefficients were not well known, they were varied randomly over a range to test transport sensitivity. To account for boulders with different aspect ratios, the three axes were related according to: $(a, b, c) = (C_{nc}b_0, b_0, b_0/C_{nc})$, where b_0 was the nominal axis size, and $C_{nc} = 1.0 + 0.5R_{nc}$ provides a random variation for boulder shapes. The coefficient R_{nc} (like other similar $R_{(-)}$ factors) represents a random number that is specific for the parameter C_{nc} (or more generally a parameter $(-)$), and is taken from a uniform $[0, 1]$ distribution. Boulder volumes were then computed from the three principal axis lengths as

$$\mathrm{Vol}_0 = 0.5abc(0.9 + 0.2R_v) = 0.5C_v abc, \tag{7}$$

where the 0.5 factor accounted for boulder shapes that are not rectangular prisms [Engel and May, 2012], and the factor $C_v = (0.9{+}02R_v)$ provided a random variation about the mean. The submerged volume (used to compute buoyancy) was similarly given as $\mathrm{Vol}_s = 0.5a(0.5b\min(c, h+\eta) + 0.5c\min(b, h+\eta))(0.9 + 0.2R_v)$, which assumes that there is an equal chance of either the b or c axes being vertical.

Again because of irregular shapes, the submerged frontal area, A_s, was given as $A_s = 0.7C_v^{2/3} a \min(h+\eta, c)$ when the particle was stationary (indicating that the boulder has its narrowest (c) axis vertical, and with reduction factors for nonrectangular frontal area), and $A_s = 0.7C_v^{2/3} a(0.5\min(h+\eta, c) + 0.5\min(h+\eta, b))$ when the boulder was in motion, assuming that either the b or c axis may be vertical.

Other parameters were also given random variations that changed with each run: Other parameters were also given variations as shown below, where all coefficients $R(-)$ are again uniform random coefficients specific to that coefficient taken from $[0, 1]$, and all $R_{(-)}$ changed for each boulder.

$$\begin{aligned}
\mu_0 &= 0.75(0.7 + 0.6R_{\mu 0}),\\
\mu_d &= 0.75(0.4 + 0.4R_{\mu d}),\\
C_d &= 1.05(0.7 + 0.6R_{Cd}),\\
C_m &= 2.5(0.7 + 0.6R_{Cm}),\\
C_l &= 0.178(0.7 + 0.6R_{Cl}),\\
\rho_s &= 2300(0.9 + 0.2R_\rho).
\end{aligned} \tag{8}$$

All friction coefficients were multiplied by 1.5 for $120\,\mathrm{m} < x < 180\,\mathrm{m}$, and by 2.0 for $x > 180\,\mathrm{m}$, to account for the greater concentration of vegetation in these regions. A major source of uncertainty in these simulations is that quantities like frictional coefficients, and random variations in all coefficients, were chosen on the basis of engineering judgment, and there exists little data to either support or refute their ranges.

Five boulder classes were used during this modeling study, corresponding to different size ranges. These classes used $D = 0.5$, 1, 2, 3, and 4 m length scales; however the relative lengths of the three axes (boulder shape) varied as discussed previously. Although it is clear from field data that boulders had different initial locations, this proved difficult to estimate quantitatively as the vast majority of boulders were not visible in pre-storm satellite photographs. Thus, all boulders were specified to become mobile at the beginning of the storm at $x = -25\,\mathrm{m}$, just offshore of the shoreline; as several large boulders were observed in this region from pre-storm satellite photos as seen in Fig. 6 (some runs varied initial position as described below). For each hydrodynamic simulation, 20 boulders with random characteristics as detailed above were initialized in each of the size classes. Since there were 20 different hydrodynamic simulations, this gave 400 simulations in each size class, enough that some statistics could be obtained.

4. Estimation of Storm Hydrodynamics from Boulder Characteristics

Figure 10 and Table 1 show individual cross-shore locations for all boulders measured in the field, in addition to mean modeled boulder terminal positions. Smaller boulders were both predicted and observed to be much more mobile, with distance traveled decreasing as boulder sizes increased: the smallest class, $D = 0.5\,\mathrm{m}$, was

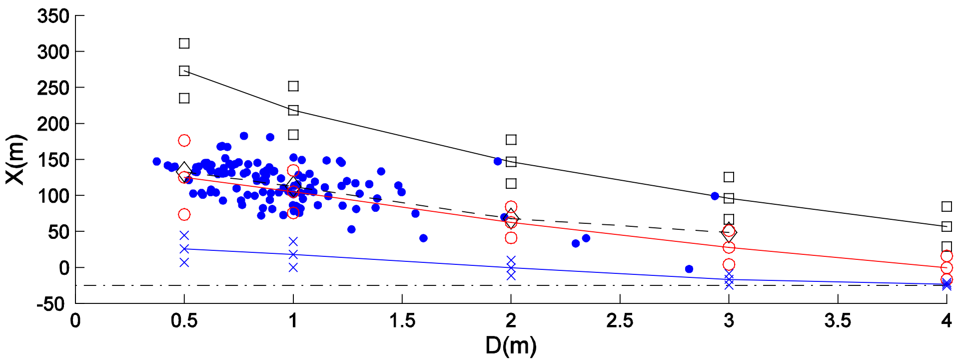

Fig. 10. Computed and measured terminal locations for boulders with varying sizes. (•) Individual Measured; (-◊-) Measured Binned Means; (□) Computed ±1 standard deviation using 1.0 Hs; (o) Computed ±1 standard deviation using 0.75 Hs; (x) Computed ±1 standard deviation using 0.5H s; (-·-) Initial location.

Table 1. Statistics of modeled (400 samples for each boulder size) and observed boulder transport for different size classes.

Boulder class	D Range (m) (number measured)	Modeled minimum, mean, maximum, and standard deviation of Boulder Terminal Positions (m)			
		H_s	$0.75H_s$	$0.5H_s$	Observed
1	0.26–0.75 m (38)	176, 273, 356, 38	2, 125, 229, 52	0, 26, 51, 19	93, 133, 168, 19
2	0.75–1.5 m (72)	131, 218, 296, 34	41, 105, 186, 30	−2, 18, 56, 18	53, 112, 183, 26
3	1.5–2.5 m (6)	73, 147, 218, 30	1, 62, 121, 21	−25, −1, 34, 11	33, 68, 147, 43
4	2.5–3.5 m (2)	7, 96, 165, 29	−23, 27, 78, 23	−25, −17, 5, 8	−2, 48, 99, N/A
5	>3.5 m (0)	−18, 57, 121, 28	−25, −1, 45, 16	−25, −24, −12, 2	N/A

computed to have average terminal position of $x = 264$ m (inland from the shoreline), while the largest class of $D = 4$ m showed far less mobility with a mean terminal position of $x = 54$ m. Variations in boulder properties such as friction and drag coefficients proved to be much less important than overall boulder size and wave-heights in predicting mobility, suggesting that as long as reasonable values are used, model results will fall within a relatively small range. However, modeled transport using hindcast wave properties significantly exceeded observed values as seen in Fig. 10. There could be many reasons for this. The first, and most obvious, is that the input significant wave-heights may have errors due to the wave model and complex local bathymetric effects. Other important considerations include the 1D nature of the Boussinesq simulation, the inability of the model to represent effects of obstructions that were observed to limit transport in many instances, and uncertainty in coefficients used to model transport. The unknown times and locations when boulders detached from the headland or were uncovered by erosion adds to the modeling uncertainty.

Boulder transport simulations using 0.75 and 0.5 times the hindcast wave-heights were also conducted, with results shown in Fig. 10 and Table 1. These distances traveled are considerably lower, and results using $0.75H_s$ show much closer agreement with the bulk of measurements. Results using $0.5H_s$ show a continuing decrease in distance traveled, with predicted travel much less than observations. Thus, transport distance is highly sensitive to incident wave properties and a knowledge of boulder terminal positions may be able to provide a rough constraint on storm magnitudes when other information is not available. This has the potential to yield more accurate information about wave-heights than initiation of motion criteria [Nott, 2003; Nandasena *et al.*, 2011] because the distance traveled is seen to be a strong function of incident wave-height even when boulders are strongly mobile. This sensitivity arises not only because orbital and bore velocities increase strongly with wave-height, but also runup distance [Stockdon *et al.*, 2006] — swash from smaller waves may not even reach locations where larger waves may deposit boulders.

It is well known from the coastal science and engineering literature that inner surf zone and swash motions often follow infragravity time scales rather than the scales of the incident waves, and can feature swiftly advancing bore inundation over

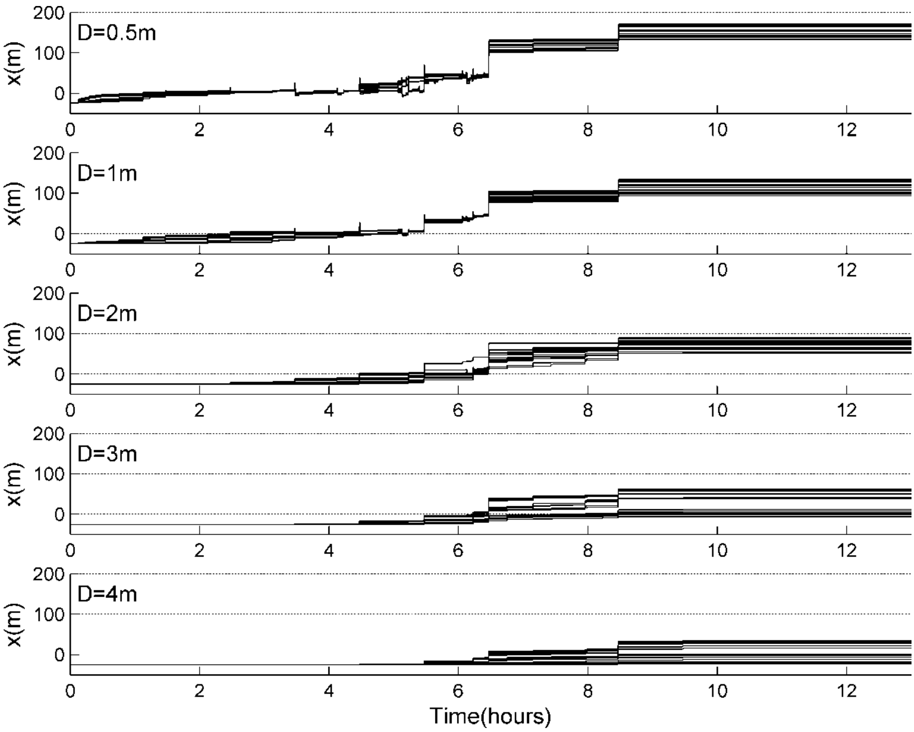

Fig. 11. Time series of motion for different boulder sizes over Haiyan simulation using 0.75 Hs. Different lines show range of motion using same hydrodynamics but with 20 different random boulder properties as described in the text.

dry beds, with slower retreating fronts [Nwogu and Demirbilek, 2010]. Figure 11 shows computed motion over a single realization of storm hydrodynamics for all boulder size classes, using 20 random realizations of boulder properties and initial position $x = -25$ m. Onshore transport is seen for all size classes and arises from the asymmetry of velocities and depths at the bore front. Both loading and motion are seen to be extremely episodic, as static friction was exceeded by mobilizing forces only in the largest swash bores. The smallest boulder class with $D = 0.5$ m was the exception to this, and shows strong mobility in both uprush and downwash motions while near sea level. Transport for all boulder sizes became increasingly intermittent with distance shoreward, and boulders at higher elevations were only inundated a small fraction of the time. For these shoreward locations, only very large infragravity swash bores could even reach the boulders, and the ground remained dry for the majority of the time. When mobilized, the boulders tended to move shoreward for a short time and then remain motionless for minutes to hours until the next large runup bore reached their locations. Larger boulders showed far more intermittency in motion than smaller boulders, with the $D = 4$ m class only mobilized by a few discrete events.

Although boulders had different random properties, motion paths were fairly similar for each size class. This is encouraging, and suggests that some error in the estimation of, for example, drag coefficient, may not present a fatal obstacle to boulder transport modeling if hydrodynamics are reasonably well known. However, the largest two boulder classes, $D = 3\,\text{m}$ and $D = 4\,\text{m}$, did show more variance in final position: as these large boulders were much less mobile, relatively small changes in boulder properties might lead to a nonmobile boulder becoming mobile or vice-versa. Moreover, motion of these large boulders was mainly influenced by a few large runup bores; thus the accurate modeling of hydrodynamics and infragravity waves is also of greatest importance for boulders on the cusp of mobility.

For boulders on slopes, gravitational forces acting downslope were typically 10–15% of frictional forces, but played a significant role in preventing upward motion on steeper slopes. Drag was the largest mobilizing force, while inertia increased in importance as boulder diameters increased: for a one hour simulation using $0.75H_s^{\max}$, ratios were $F_{i\text{RMS}}/F_{d\text{RMS}} = [0.15, 0.22, 0.36, 0.52, 0.58]$. This importance

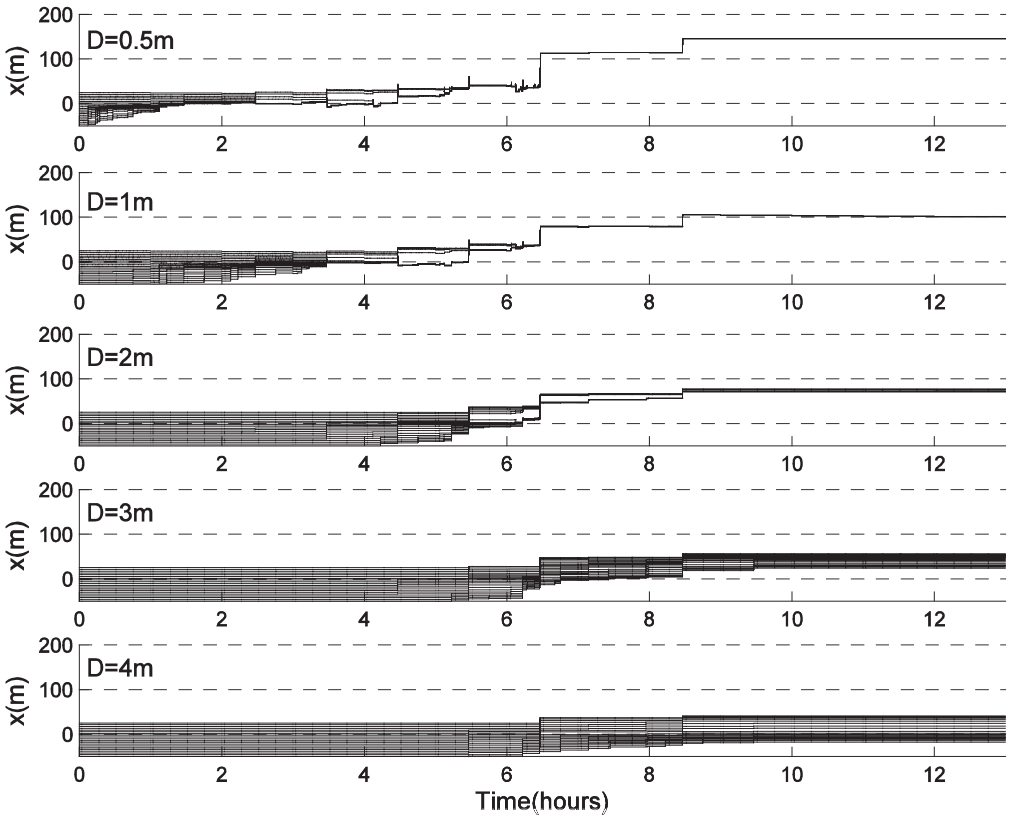

Fig. 12. Time series of motion for different boulder sizes over Haiyan simulation using 0.75 Hs. Different lines show range of motion using same hydrodynamics and same boulder properties, but with 20 different start locations evenly spaced from −50 m to 25 m.

of inertia for larger boulders is not in accord with many other studies, which tend to assume that inertial forces are "relatively insignificant" [Nott, 2003]. However, bore fronts in the surf and swash zones have large accelerations which become increasingly important in the transport of larger boulders, as might also be expected from an examination of Keulegan–Carpenter numbers [e.g. Dean and Darymple, 1991].

4.1. *Initiation of motion criteria*

One of the main goals of boulder transport analysis is to recreate details of unknown historical storms or tsunamis using observed boulder locations and characteristics. The most common techniques used for this are the various initiation of motion criteria [Nott, 2003; Nandasena *et al.*, 2011]. These use measured boulder (a, b, c) length scales and density combined with the assumption of a drag-dominated system and estimates of quantities such as drag and frictional coefficients to arrive at the velocities required to initiate either sliding or rolling motion. A secondary step often estimates either storm wave or tsunami wave-heights from the inferred maximum velocities. For a boulder shaped like a rectangular prism, the Nandasena corrections to Nott's equations give the inferred velocity at the initiation of sliding

$$U_{\text{slide}}^2 \geq \frac{2gc(\rho_s/\rho_w - 1)(\mu\cos\theta + \sin\theta)}{C_d(c/b) + \mu C_l}. \tag{9}$$

For the initiation of overturning,

$$U_{\text{roll}}^2 \geq \frac{2gc(\rho_s/\rho_w - 1)(\cos\theta + (c/b)\sin\theta)}{C_d(c^2/b^2) + C_l}. \tag{10}$$

Comparisons between inferred velocities to move field-measured boulders and modeled Boussinesq velocities at different cross-shore locations are given in Fig. 13. Particularly for the sliding mode, inferred velocities tend to be significantly less than modeled velocities using $0.75H_s$, which gave the best overall comparison for transport distances. However, because of the uncertainty in wave-heights, it is difficult to make strong conclusions here. A more direct comparison uses inferred velocities for modeled boulders and compares them to Boussinesq maximum velocities at different cross-shore locations. Because the Boussinesq wave model provided the depths and velocities used to drive boulder transport, and because all coefficients used in the model simulations are known, this provides a direct evaluation of the accuracy for initiation of motion criteria when compared to a more complex dynamical model. Figure 9 thus also shows bin-averaged inferred fluid velocities to initiate sliding and rolling for modeled boulders. As with the field boulders (whose mean velocities are close to the means of the modeled boulders) maximum Boussinesq velocities at a site tend to significantly exceed estimates using initiation of motion criteria, particularly for sliding motion. This suggests that initiation of motion criteria tend to work best as a lower bound on velocities, and may significantly underestimate actual conditions encountered during a storm.

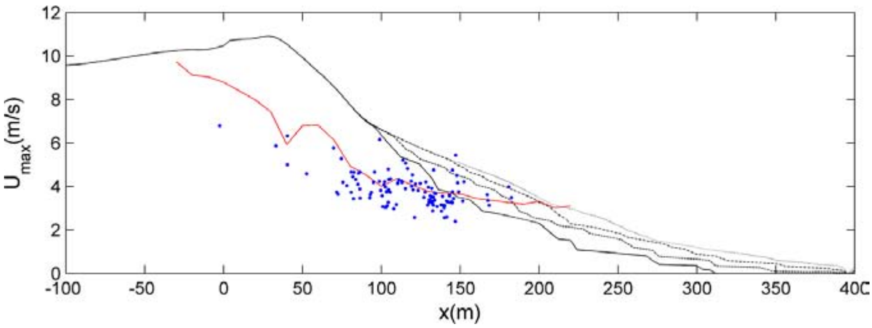

(a)

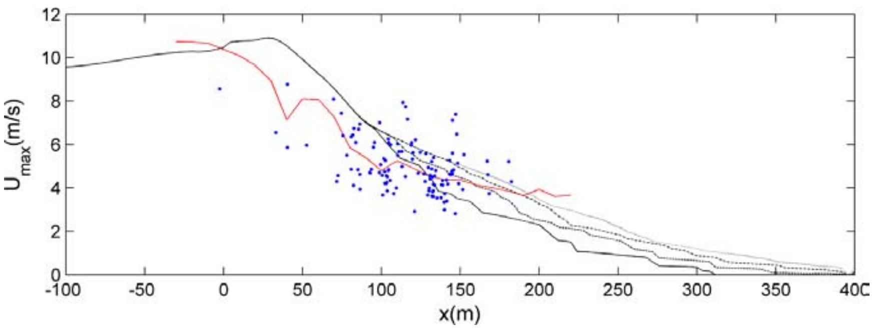

(b)

Fig. 13. Inferred fluid velocities to initiate boulder motion, plotted against onshore distance. (a) Velocities to initiate sliding; (b) Velocities to initiate rolling. (•) Inferred velocities from observed boulders. (—) Average inferred sliding and rolling velocities from numerical boulder transport, averaged in 10 m bins. Black lines are maximum fluid velocities over the storm taken directly from Boussinesq model outputs using 0.75 Hs, for instantaneous depths greater than (from top) [0.5, 1, 2, 3] m, averaged over 20 model runs.

This data may be seen differently in Fig. 14, where inferred velocities for modeled boulders are individually compared to Boussinesq maximum velocities at the modeled terminal boulder positions. Again, it is clear that initiation of velocity criteria are very much lower bound: all $D = 0.5$ m boulders have inferred velocities to initiate sliding less than actual maximum velocities at their terminal location, while the percentage is 99.5% for inferred rolling velocities. These underpredictions decrease with increasing boulder size: for $D = 3$ m boulders, only 88% of inferred sliding velocities are underpredicted, while 53% of inferred rolling velocities are underpredicted. For small boulders, errors likely arise from the short durations of maximum velocities, which do not allow boulders to move as far inland as they might with a more steady current. For large boulders, inertial forces are considered to be "relatively insignificant" [Nott, 2003] in the initiation of velocity criteria but are important in modeled transport: this means that modeled boulders can actually be transported with lower velocities than if just drag were considered, leading to

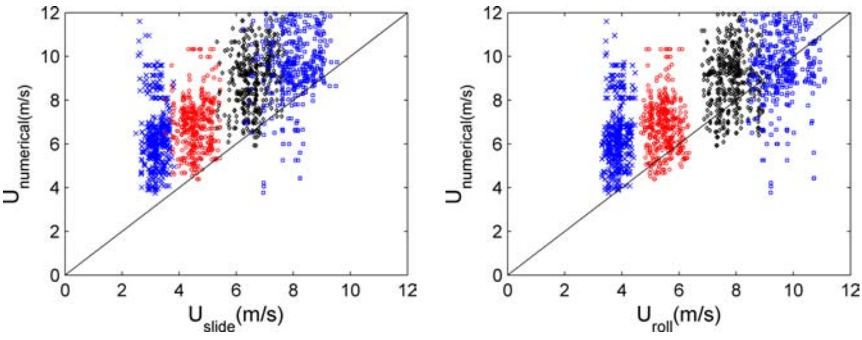

(a) (b)

Fig. 14. Comparison between maximum Boussinesq numerical velocities $\mathrm{U_D}$ at boulder end locations at times when $(h+\eta) \geq D$, and inferred (a) sliding, and (b) rolling velocities for all numerically simulated boulders. (x) $D = 0.5$ m; (o) $D = 1$ m; (◊) $D = 2$ m; (□) $D = 3$ m.

a smaller difference between inferred and recorded velocities. For all cases, mean modeled velocities at the terminal positions are much greater than mean inferred velocities.

4.2. *Wave loads*

For near-coast structures, boulder transport has relevance largely because it shows where historical inundation with high velocities has taken place. Estimates of the loads required to transport boulders with given size, shape, and density provide additional constraints on the hydrodynamics. Together, these have the potential to estimate the historical loading climate in a given location, which may then be used to inform planning and design. No field data will be used in this section to facilitate a more direct comparison between inferred and modeled quantities — all estimates arise from inferred maximum velocities using (9), which are then used to estimate drag forces. At the final resting place of a modeled boulder, the inferred drag force potential per unit width may be calculated from the square of the inferred velocity multiplied by the depth at the time of maximum velocity. This is sometimes referred to as the momentum flux parameter [e.g. Linton *et al.*, 2013] and is given here by $U^2(h+\eta)$. For inferred forces, two choices are used for the depth scale. The first takes the depth as the boulder height, which here is the shortest axis dimension:

$$\frac{F_{\text{inferred}}}{0.5\rho C_d w} = cU_{\text{slide}}^2. \tag{11}$$

An alternate depth scale suggests itself from the often-used incipient motion assumption that the Froude number of wave flows is one [e.g. Nott, 2003]. This leads to a depth of $(h+\eta) = U^2/g$ and thus

$$\frac{F_{\text{inferred}}}{0.5\rho C_d w} = U_{\text{slide}}^4/g. \tag{12}$$

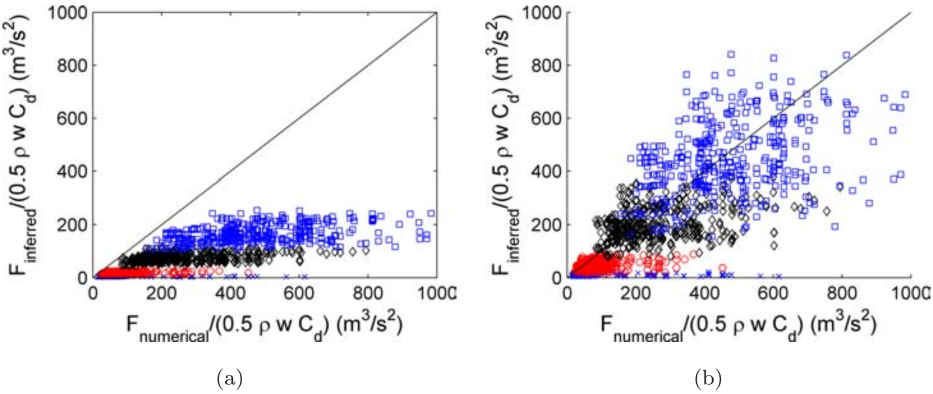

Fig. 15. Maximum numerical drag force potential over entire storm, evaluated at numerical boulder terminal position ($F_{\mathrm{numerical}}$), compared to force potential from inferred sliding velocities and boulder properties (F_{inferred}). Different colors indicate different classes of numerical boulders (x) $D = 0.5$ m; (o) $D = 1$ m; ($\Diamond$) $D = 2$ m; ($\Box$) $D = 3$ m. The solid black line indicates 1:1 correspondence. (a) Inferred forces using boulder length scale from c-axis; (b) Inferred forces using a Froude number of unity.

Maximum drag force estimates may also be found directly from model outputs, as the maximum of the depth-integrated momentum flux over time at the terminal boulder position,

$$\frac{F_{\mathrm{numerical}}}{0.5\rho C_d w} = (U^2(h+\eta))_{\max}. \tag{13}$$

Figure 15 compares inferred and modeled drag force potentials at the modeled terminal boulder locations. When the boulder height is used as length scale (11), modeled loads in all cases greatly exceed inferred loads, often by many multiples, and in no cases are the modeled loads less than inferred loads. This discrepancy arises because inferred boulder loads have no knowledge of water depths exceeding the boulder height, which appear to be significant. In contrast, estimates of loads using a Froude number of unity show significantly better correspondence with the computed hydrodynamics, particularly for the larger boulders. For $D = 2$ m and $D = 3$ m, the ratios of computed to inferred loads using (12) are 1.36 and 1.13, respectively, although there is significant scatter. Inferred loads using the smaller boulders are still poor. Clearly, a hydrodynamic-based depth estimate is much more accurate than can be found by using boulder height scales. Results here further suggest that the largest boulders moved during a storm may contain the most useful information about hydrodynamic loads, and these should be the focus of field investigations. Simple initiation of motion estimates may have some value in estimating the potential loads that might have been encountered during a storm, and could provide useful information if used prudently. However, even in this best-case scenario where all numerical coefficients used in the simulations are known exactly, scatter remains large and any designs should use a significant safety factor.

5. Discussion and Conclusions

The extreme runup from Super Typhoon Haiyan generated boulder transport to distances approaching 200 m inland. Boulder sizes decreased with increasing distance inland, although there was considerable scatter, and largest boulders in the beach region exceeded 5 m in length. Boulder sources appeared to vary: some were clearly pre-existing and either buried in the sand or resting loosely on the land surface pre-storm, while others likely became detached from highly karstified headlands during the storm. These pre-existing boulders had very likely been generated during previous events, although it was not possible to identify these events with any confidence. Boulder sizes and transport distances are in line with other descriptions of transport observed in other large storms [Khan *et al.*, 2010; Goto *et al.*, 2011], but also overlap with the size range of boulders transported by tsunamis [Goff *et al.*, 2006; Goto *et al.*, 2010; Nandasena *et al.*, 2013].

High-resolution Boussinesq modeling of boulder transport during Super Typhoon Haiyan predicted motion driven by infragravity swash bores, causing highly episodic travel in the case of larger boulders ($D > 1$ m). Once onshore, transport was almost exclusively shoreward, causing boulders to be stranded. The inland distance traveled was found to be a strong function of the incident wave-height and the boulder size. Storms with larger waves led to much greater distances traveled than storms with smaller waves. Uncertainty in parameters such as drag and friction coefficients played a much smaller role in determining terminal locations. Predictions of boulder transport using hindcast wave-heights showed transport further inland than was observed, but slightly smaller wave-heights produced good agreement. Inertial forces were non-negligible, with the importance of inertia increasing with boulder diameter.

Simulations also gave an opportunity to compare velocities that were used to drive the boulder transport model with inferred velocities from widely used initiation of motion criteria. Inferred velocities were almost always significantly underpredicted when compared to the actual velocities in the model at the terminal boulder location. This indicates that inferred velocities [e.g. Nandasena *et al.*, 2011] are very much of a lower bound as shown in Fig. 14, particularly for smaller boulder sizes.

Inferred drag loads using boulder height as a depth scale gave very poor results, and should not be used. Inferred loads using a Froude number of unity to estimate depth gave much better results, particularly for the largest boulders. However, although inferences were able to estimate order of magnitude loads, they had poor precision. Knowing this, it might be possible to apply safety factors to provide conservative results, but any implementation would require considerably more research.

Models suitable for computing detailed time series of inundation are relatively well developed and, given incident wave conditions and detailed bathymetry, should be able to compute reasonably the storm wave or tsunami hydrodynamics at these locations. Models for computing detailed boulder motion are significantly less developed, and should be a focus of future research. Processes that could benefit from improvements include local obstructions that prevent boulder transport, boulder generation from rock masses, or breakage during the storm, shoreline erosion leading to buried boulder mobility, and quantification of the modes of travel, whether from sliding, rolling, or saltation. The 1D nature of the present simulations may also prove a limit to fidelity, and 2D simulations should be explored in the future. However, the overall hydrodynamic-boulder model appeared to provide an advance in the detailed description of boulder transport during strong storms.

At the largest scale, events like the 2011 Great East Japan Tsunami can transport larger blocks greater distances than may be possible from storm waves [Nandasena *et al.*, 2013; Goto *et al.*, 2014]. However, the tsunami literature sometimes discounts the competence of storm waves to transport boulders long distances, which may lead to misdiagnosis of boulder origins. For example, applying Eq. (1) of Lorang [2011] to the conditions at Calicoan Island leads to estimates of 1–2 m final elevation for a 2 m diameter boulder, which is far less than was observed. The present work demonstrates that the potential to transport large boulders far onshore to high inland elevations does not lie exclusively with tsunamis, but can also be achieved by strong tropical cyclones. Because swash hydrodynamics vary strongly with inland distance, estimates of paleostorm intensities might profitably use boulder terminal positions to constrain hydrodynamics and thus wave-heights through modeling exercises similar to those presented here. Regions of tsunami and tropical cyclone hazards overlap in the Philippines, South of Japan, Indonesia, Samoa and many other areas. Analysis of existing boulders in these regions should carefully consider both types of events.

Finally, the intermittent loading of boulders onshore by swash bores has direct implications for loading on manmade structures, which may be located in similar regions and will experience similar forces. This type of loading is generally not considered in existing codes and standards, but should be a priority for future studies.

Acknowledgments

This work was funded under NSF grants 1426445, 1025519, and 1435007, by ONR grants N00014-11-1-0045 and N00014-13-1-0123, and the Japan Society for the Promotion of Science Kakenhi grant. We appreciate survey support by the American Society of Civil Engineers, the Japan Society of Civil Engineers, the Philippine Institute of Civil Engineers, and the Department of Public Works and Highways of the Philippines. Valerie Ambait and Nile April Robino provided significant logistical assistance to the field campaign.

References

Booij, N., Holthuijsen, L. H. & Haagsma, I. J. G. [1998] "Comparing the second-generation HISWA wave model with the third-generation SWAN wave model," in *Proc. 5th Int. Workshop on Wave Hind. and Forecasting*, pp. 215–222.

Bourgeois, J. & MacInnes, B. [2010] "Tsunami boulder transport and other dramatic effects of the 15 November 2006 central Kuril Islands tsunami on the island of Matua," *Z. Geomorphol.* **54**(S3), 175–195.

Buckley, M. L., Wei, Y., Jaffe, B. E. & Watt, S. G. [2012] "Inverse modeling of velocities and inferred cause of overwash that emplaced inland fields of boulders at Anageda, British Virgin Islands," *Nat. Hazards* **64**, 133–149.

Cardone, V. J., Callahan, B. T., Chen, H., Cox, A. T., Morrone, M. A. & Swail, V. R. [2015] "Global distribution and risk to shipping of very extreme sea states (VESS)," *Int. J. Climatol.* **35**(1), 69–84.

Dean, R. G. & Darymple, R. A. [1991] *Water Wave Mechanics for Engineers and Scientists*, World Scientific, Singapore.

Engel, M. & May, S. M. [2012] "Bonaire's boulder fields revisited: Evidence for Holocene tsunami impact on the Leeward Antilles," *Quat. Sci. Rev.* **54**, 126–141.

Fichaut, B. & Suanez, S. [2011] "Quarrying, transport and deposition of cliff-top storm deposits during extreme events: Banneg Island, Brittany," *Mar. Geol.* **283**, 36–55.

Goff, J., Dudley, W. C., deMaintenon, M. J., Cain, G. & Coney, J. P. [2006] "The largest local tsunami in 20th century Hawaii," *Mar. Geol.* **226**, 65–79.

Goto, K., Okada, K. & Imamura, F. [2010] "Numerical analysis of boulder transport by the 2004 Indian Ocean tsunami at Pakarang Cape, Thailand," *Mar. Geol.* **268**, 97–105.

Goto, K., Kunimasa, M., Kawana, T., Takahashi, J. & Imamura, F. [2011] "Emplacement and movement of boulders by known storm waves — Field evidence from the Okinawa Islands, Japan," *Mar. Geol.* **283**, 66–78.

Goto, K., Sugawara, D., Ikema, S. & Miyagi, T. [2014] "Sedimentary processes associated with sand and boulder deposits formed by the 2011 Tohoku-oki tsunami at Sabusawa Island, Japan," *Sediment. Geol.* **282**, 188–198.

Husana, D. E. & Yamamuro, M. [2013] "Groundwater quality in karst regions in the Philippines," *Limnology* **14**(3), 293–299.

Imamura, F., Goto, K. & Ohkubo, S. [2008] "A numerical model for the transport of a boulder by tsunami," *J. Geophys. Res.* **113**, C01008.

Joint Typhoon Warning Center [2013] "Haiyan best track," Available at http://www.usno.navy.mil/NOOC/nmfc-ph/RSS/jtwc/best_tracks/2013/2013s-bwp/bwp312013.dat.

Khan, S., Robinson, E., Rowe, D.-A. & Coutou, R. [2010] "Size and mass of shoreline boulders moved and emplaced by recent hurricanes, Jamaica," *Z. Geomophol.* **54**(S3), 281–299.

Kim, S. Y., Yasuda, T. & Mase, H. [2009] "Numerical analysis of effects of tidal variations on storm surges and waves," *Appl. Ocean Res.* **30**(4), 311–322.

Lorang, M. S. [2011] "A wave-competence approach to distinguish between boulder and megaclast deposits due to storms waves vs tsunami," *Mar. Geol.* **283**, 90–97.

Linton, D., Gupta, R., Cox, D., van de Lindt, J., Oshnack, M. E. & Clauson, M. [2012] "Evaluation of tsunami loads on wood-frame walls at full scale," *J. Struct. Eng.* **139**(8), 1318–1325.

Mori, N., Kato, M., Kim, S., Mase, H., Shibutani, Y., Takemi, T., Tsuboki, K. & Yasuda, T. [2013] "Local amplification of storm surge by Super Typhoon Haiyan in Leyte Gulf," *Geophys. Res. Lett.* **41**, doi:10.1002/2014GL060689.

Nandasena, N. A. K., Paris, R. & Tanaka, N. [2011] "Reassessment of hydrodynamic equations: Minimum flow velocity to initiate boulder transport by high energy events (storms, tsunamis)," *Mar. Geol.* **281**, 70–84.

Nandasena, N. A. K., Tanaka, N., Sasaki, Y. & Oda, M. [2013] "Boulder transport by the 2011 Great East Japan tsunami: Comprehensive field observations and whither model predictions?" *Mar. Geol.* **346**, 292–309.

Nott, J. [2003] "Waves, coastal boulder deposits and the importance of the pre-transport setting," *Earth Planet. Sci. Lett.* **210**, 269–276.

Nwogu, O. & Demirbilek, Z. [2010] "Infragravity wave motions and runup over shallow fringing reefs," *J. Waterway Ports Harbor Coastal Ocean Eng. ASCE* **136**, 295–305.

Shimozono, T., Tajima, Y., Kennedy, A. B., Nobuoka, H., Sasaki, J. and Sato, S. [2015] "Combined infragravity wave and sea-swell runup over fringing reefs by super typhoon Haiyan," *J. Geophys. Res. – Oceans* **120**, doi:10.1002/2015JC010760.

Skamarock, W. C., Klemp, J. B., Dudhia, J., Gill, D. O., Barker, O. M., Duda, M. G., Huang, X. Y., Wang, W. & Powers, J. G. [2008] "A description of the Advanced Research WRF Version 3," NCAR Tech. Note, 475, p. 113.

Stockdon, H. F., Holman, R. A., Howd, P. A. & Sallenger, A. H. [2006] "Empirical parameterization of setup, swash, and runup," *Coastal Eng.* **53**, 573–588.

Sugawara, D., Goto, K. & Jaffe, B. E. [2014] "Numerical models of tsunami sediment transport — Current understanding and future directions," *Mar. Geol.* **352**, 295–320.

Tajima, Y., Yasuda, T., Pacheco, B. M., Cruz, E. C., Kawasaki, K., Nobuoka, H., Miyamoto, M., Asano, Y., Arikawa, T., Ortigas, N., Aquino, R., Mata, W., Valdez, J. & Briones, F. [2014] "Initial report of JSCE-PICE joint survey on the storm surge disaster caused by Typhoon Haiyan," *Coastal Eng. J.* **56**, 1450006.

Zhang, Y., Kennedy, A., Panda, N., Dawson, C. & Westerink, J. J. [2013] "Boussinesq–Green–Naghdi rotational water wave theory," *Coastal Eng.* **73**, 13–27.

Zhang, Y., Kennedy, A. B., Donahue, A., Westerink, J. J., Panda, N. & Dawson, C. [2014] "Rotational surf zone modeling for O(μ^4) Boussinesq–Green–Naghdi systems," *Ocean Model.* **79**, 43–53.